ACS APPLIED MATERIALS & INTERFACES

www.acsami.org

Research Article

Polyimide Nanofiber-Reinforced $Ti_3C_2T_x$ Aerogel with "Lamella-Pillar" Microporosity for High-Performance Piezoresistive Strain Sensing and Electromagnetic Wave Absorption

Lei Pu, Yongpeng Liu, Le Li, Chao Zhang, Piming Ma, Weifu Dong, Yunpeng Huang,* and Tianxi Liu*

Cite This: *ACS Appl. Mater. Interfaces* 2021, 13, 47134–47146

Read Online

ACCESS | Metrics & More | Article Recommendations | Supporting Information

ABSTRACT: Assembling two-dimensional MXenes into 3D macroscopic structures is an applicable method to give full play to its excellent electrical and mechanical properties toward multifunctionality. Considering the weak interfacial interaction and poor gelation ability of MXenes, short polyimide nanofibers (PINFs) are utilized as cross-linking and supporting building blocks in this work to construct a lightweight, robust, and elastic PINF/$Ti_3C_2T_x$ MXene composite aerogel (PINF/MA) via a simple synergistic assembly strategy. Taking advantage of its unique 3D "lamella-pillar" microporous architecture, the designed PINF/MA composite aerogel exhibits excellent piezoresistive sensing performance in terms of a wide pressure range of 0–8 kPa (50% strain), a high piezoresistive sensitivity of 22.32 kPa^{-1}, an ultra-low detection limit of 0.1% strain, and great compression/rebound stability (signal remained stable after 1500 cycles). These remarkable piezoresistive sensing properties enable the PINF/MA with intriguing capability to detect small and large human activities in real time (wrist and finger bending, pulse, and vocal cord vibration). More interestingly, the parallelly aligned leaf vein-like lamellae also empower the PINF/MA with prominent wave absorption performance [RL_{min} is −40.45 dB at 15.19 GHz, with an effective absorption bandwidth of 5.66 GHz (12.34–18 GHz)], making the multi-functional PINF/MA composite aerogels promising candidates for wearable strain sensors and microwave absorbers.

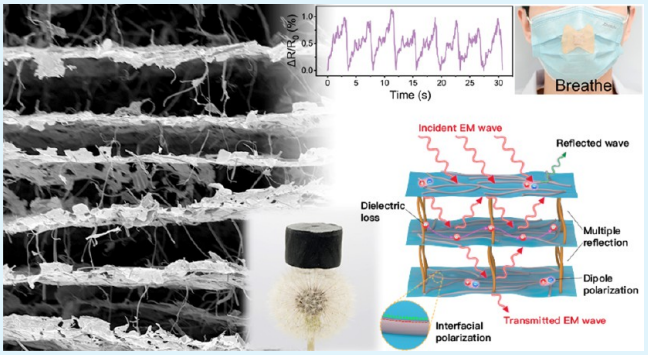

KEYWORDS: *two-dimensional nanomaterials, polyimide nanofibers, multi-functional composite aerogels, piezoresistive sensing, microwave absorption*

1. INTRODUCTION

Since Novoselov and Geim first prepared atomically thick graphene by mechanical exfoliation in 2004, two-dimensional (2D) nanomaterials have aroused widespread research interests because of their special lamellar structure and intriguing chemical/physical properties.[1] Monolayer MXene nanosheets, which were first discovered in 2011 with the chemical formula $M_{n+1}X_nT_x$ [(n = 1–4), where M represents the early transition metals, X represents C/N, and T_x denotes different functional groups],[2] have attracted worldwide attention due to their great solid–liquid processability, extraordinary electrical conductivity (6000–8000 S cm^{-1}), high aspect ratio, and highly adjustable surface chemistry derived from their metal skeleton and abundant surface functional groups.[3] In addition, MXene also exhibits great thermal conductivity and excellent mechanical strength, allowing this newly discovered 2D functional material exhibit numerous applications in energy storage materials,[4] electromagnetic interference (EMI) shielding,[5] electromagnetic microwave absorption (EMA),[6] sensors,[7] water purification,[8] gas separation, and catalysis.[9]

However, MXene flakes are easy to restack due to the in-plane covalent bonding and van der Waals interaction between adjacent flakes, leading to the significant degradation of the accessible surface area and slow transmission of electrons and ions.[10] Recently, intensive investigations have been conducted to develop 3D MXene macroporous monoliths to open up the space between MXene layers to obtain larger useable surface areas and good mechanical properties. Zhao and co-workers proposed a sacrificial template strategy to assemble MXene nanosheets into flexible 3D macroporous materials with significantly improved electrochemical properties.[4] Lu et al. reported the rational construction of an ultrathin, lightweight, and porous MXene membrane with excellent EMI perform-

Received: July 22, 2021
Accepted: September 15, 2021
Published: September 28, 2021

https://doi.org/10.1021/acsami.1c13863
ACS Appl. Mater. Interfaces 2021, 13, 47134–47146

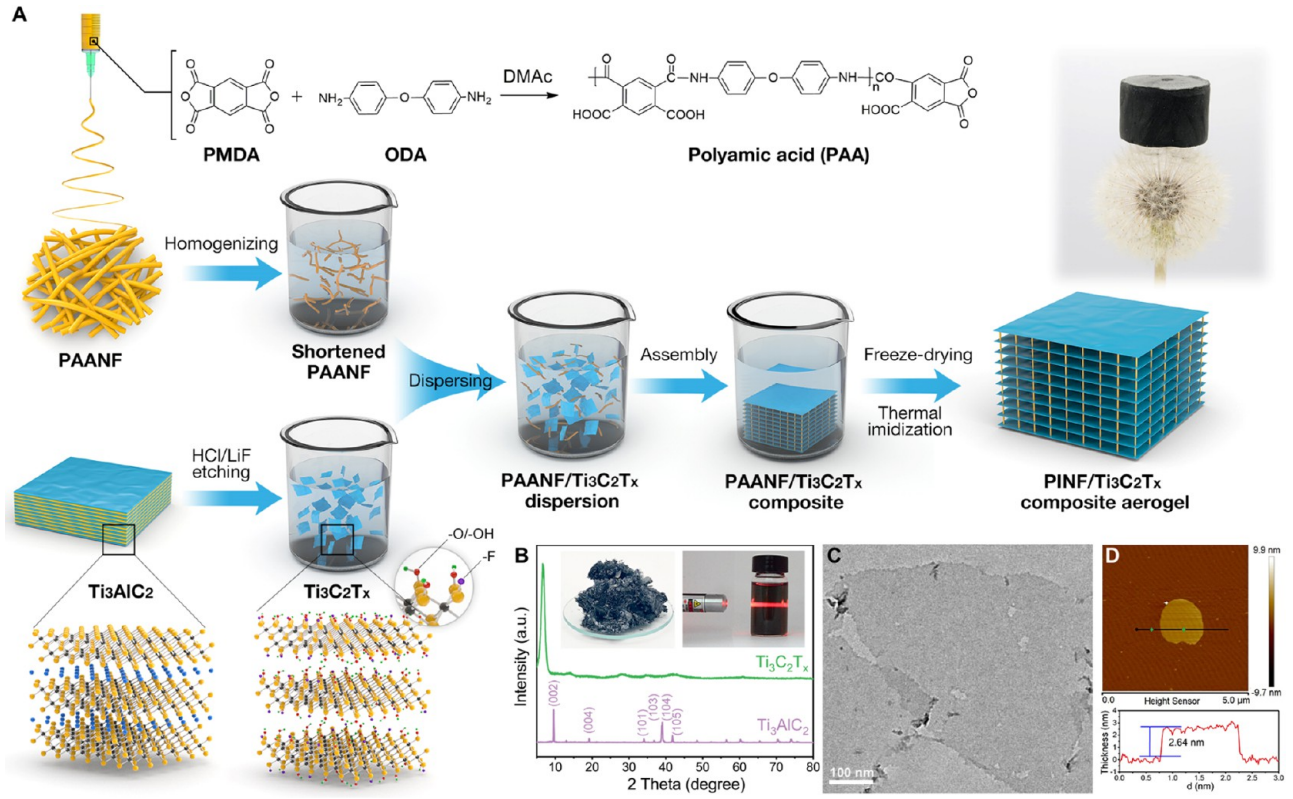

Figure 1. (A) Schematic illustration of the preparation procedure of PINF/MA composite aerogel. The photograph in the corner is a lightweight demonstration of the composite aerogel (it can stand steadily on a dandelion). (B) XRD patterns of Ti_3AlC_2 MAX and $Ti_2C_2T_x$. Insets show the photographs of freshly prepared Ti_3AlC_2 powder and the Ti_3AlC_2 aqueous dispersion. (C,D) TEM and AFM images of the synthesized $Ti_2C_2T_x$.

ance.[11] In principle, the successful construction of a 3D porous MXene network is closely related to the balance between electrostatic repulsion and bonding interactions during the assembly process.[3] However, unlike reduced graphene oxide (rGO), MXene has poor self-gelling ability; thus, it is difficult to self-assemble into an integrating 3D network.[12] Worse still, the abundant surface-active end groups (−O, −OH, and −F) cause relatively weak interactions between MXene nanosheets, which cannot effectively balance the electrostatic repulsion and prevent the MXene from self-stacking.[13] Liu and co-workers utilized the co-assembly of rGO and $Ti_3C_2T_x$ to prepare a highly interconnected MXene/rGO composite aerogel with a large specific surface area.[14] Under the synergistic effect of two building blocks, the reported composite aerogel exhibited good electronic conductivity and high acetone sensing capability. Zhang and co-workers chose carbon nanotubes (CNTs) as cross-linkers to realize the 3D construction of MXene aerogel; the prepared microporous and flexible MXene/CNT composites can effectively suppress lithium polysulfide shuttling for Li−S batteries.[15] Despite all the beneficial attempts, the fabrication of 3D MXene assemblies with excellent structural stability and multi-functionality simultaneously still remains a great challenge.

In this work, inspired by the function of pillars in building structures and the leaf vein configuration in nature, a lightweight, robust, and elastic $Ti_3C_2T_x$ MXene aerogel with unique 3D "lamella-pillar" microporous architectures is designed and fabricated through the cross-linking and intercalation of electrospun polyimide nanofibers (PINFs). In this protocol, leaf vein-like PINF/MXene lamella layers composed of few-layered $Ti_3C_2T_x$ and embedded PINFs possess superior mechanical stability and decent electrical conductivity, which are parallelly aligned and intercalated by robust PINF "pillars", resulting in the remarkable mechanical properties and multi-functionality of PINF/$Ti_3C_2T_x$ MXene composite aerogel (PINF/MA). When applied as piezoresistive strain sensors, the PINF/MA composite aerogel manifests ideal sensing performance with a wide sensing range, excellent linear sensitivity, ultra-low detection limit, and great fatigue resistance ability, which can be used to detect various human activities in real time. Furthermore, the constructed PINF/MA composite aerogel also demonstrates excellent electromagnetic microwave absorption properties. Hence, this work provides a new insight into construction of macroscopic 3D MXene assemblies for multi-functional applications.

2. EXPERIMENTAL SECTION

2.1. Exfoliation of $Ti_3C_2T_x$ Nanosheets. MXene was exfoliated through etching Ti_3AlC_2 powder (325 mesh, Jilin 11 Technology) with HCl/LiF as reported previously.[1] Typically, 2.0 g of LiF (99.0%) was first dissolved in 20 mL of HCl (6 M), and then, 2.0 g of Ti_3AlC_2 powder was added in the above solution for reaction under mild agitation at 35 °C in a water bath, and the resulting black slurry was completely washed under continuous centrifugation until the pH of the supernatant reached neutral. The obtained sediment was then dispersed in 200 mL of distilled water followed by ultrasonication in an ice bath for 1 h to obtain exfoliated $Ti_3C_2T_x$ suspension. The freshly prepared $Ti_3C_2T_x$ was dehydrated by freeze-drying for long-term preservation.

2.2. Preparation of Polyamic Acid Nanofibers. Polyamic acid nanofibers (PAANFs) were prepared through the versatile electrospinning process (Figure 1A). To begin with, PAA was synthesized via polymerization of pyromellitic dianhydride (PMDA, ≥98.5%) and 4,4′-oxidianiline (ODA, ≥98.0%) at 0 °C for 3 h under intense

https://doi.org/10.1021/acsami.1c13863
ACS Appl. Mater. Interfaces 2021, 13, 47134−47146

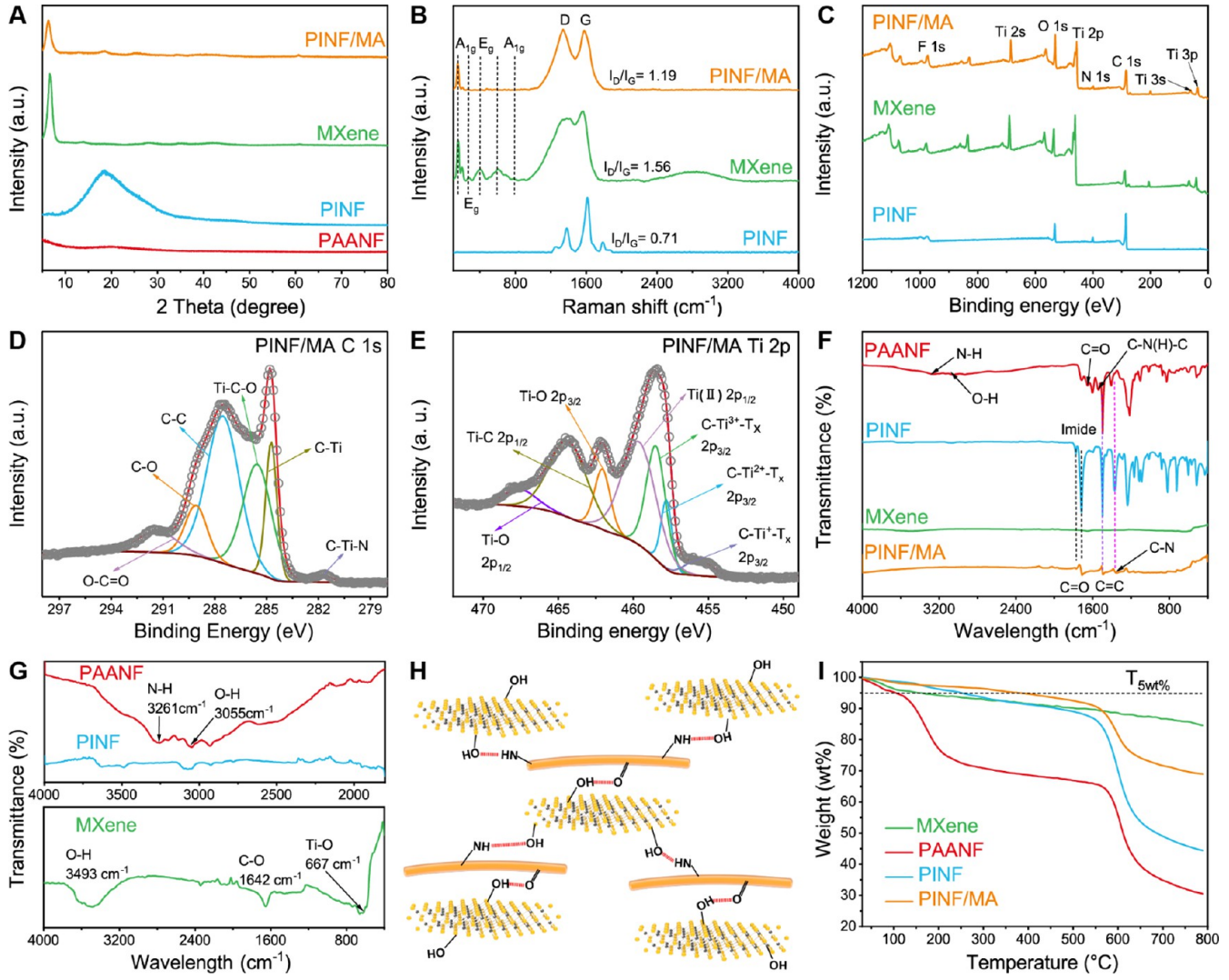

Figure 2. (A) XRD patterns of PAANFs, PINFs, MXene, and PINF/MA composite aerogel. (B) Raman spectra of PINFs, MXene, and PINF/MA composite aerogel. (C) XPS of PINFs, MXene, and PINF/MA composite aerogel. (D,E) C 1s and Ti 2p spectra of PINF/MA composite aerogel. (F,G) FT-IR spectra of PAANFs, PINFs, MXene, and PINF/MA. (H) Schematic description on the interaction between two building blocks. (I) TGA curves of different specimens.

stirring. Solution for electrospinning was prepared by diluting the resulting PAA to 8 wt % in DMF. Accept distance, applied voltage, and pumping speed were set at 20 cm, 20 kV and 0.2 mm min^{-1}, respectively. The obtained PAANF films were treated by high-speed homogenizing at 8000−10,000 rpm for 30 min to obtain a fine dispersion of short PAA nanofibers.

2.3. Construction of PINF/MXene Composite Aerogels. First of all, 0.06 g of exfoliated $Ti_3C_2T_x$ powder was dispersed in 10 mL of distilled water under sonication to prepare a stable MXene suspension, and then, 0.06 g of PAANFs was added to the above suspension and treated with a homogenizer at 8000−10,000 rpm for 10 min to realize the complete blending of two building blocks, followed by 30 min ultrasonication and 5 h mild magnetic stirring to achieve the homogeneously mixed dispersion of PAANF/MXene. Afterward, 10 mL of the above mixture was transferred to a polypropylene cylinder mould (20 × 50 mm^2) and frozen in a −120 °C ethanol refrigerant, followed by freeze-drying (−80 °C and 0.1 mbar) to achieve PAANF/MXene aerogels, which were further imidized at 300 °C for 2 h to prepare PINF/$Ti_3C_2T_x$ MXene composite aerogel (PINF/MA). For comparison, pure PINF assembly was also obtained by freeze-drying of pure PINF dispersion.

2.4. Characterizations. The microstructures of the aerogels were characterized using FESEM (Hitachi, S4800). Transmission electron microscopy (TEM) observation was conducted using a JEM-2100 plus transmission electron microscope (Japan). Atomic force microscopy (AFM) was performed on a MultiMode 8 system (Bruker). Fourier transform infrared (FTIR) analysis in a range of 500−3800 cm^{-1} was performed with a Nicolet Nexus 870 instrument. Raman tests were conducted on a 532 nm laser (Renishaw inVia Reflex). X-ray diffraction (XRD) was performed on a Bruker D8 X-ray diffractometer with a Cu Kα X-ray source (λ = 1.5418 Å). X-ray photoelectron spectroscopy (XPS) spectra were recorded on ESCA 2000 (VG Microtech, U.K.). Thermogravimetric analysis (TGA) was performed on a TGA/DSC1/1100SF system under a N_2 atmosphere. A contact angle goniometer (OCA15EC) was employed to measure the water contact angles. All infrared images were taken with a thermal camera (Fluke Ti400+, USA).

The compressive properties of PINF/MXene composite aerogel were tested with an electronic universal testing machine (UTM2203, Shenzhen Suns Technology). A digital precision multimeter (Tektronix DMM6500) was employed to measure the resistance/current changes of the samples. The $I-V$ curves and response time were measured using an electrochemical workstation (CHI-660E, Shanghai Chenhua Instrument). The electromagnetic parameters of the composite aerogel were measured on a vector network analyzer (Agilent 8720ET) at 0.5−18 GHz. Thermal conductivity was

https://doi.org/10.1021/acsami.1c13863
ACS Appl. Mater. Interfaces 2021, 13, 47134−47146

measured with a Hot Disk TPS 2500 S instrument, coupled with a hot disk kapton sensor (5501, radius 6.4 mm) sandwiched between pairs of quadrate samples with a size of 20 × 20 × 20 mm^3.

3. RESULTS AND DISCUSSION

The detailed fabrication process of PINFs, monolayer $Ti_3C_2T_x$ MXene nanosheets, and their composite aerogels is schematically described in Figure 1A. At first, Ti_3AlC_2 (MAX) powder was etched in HCl/LiF mixtures at 35 °C for 24 h, when Al in Ti_3AlC_2 was removed leaving the surface groups −F, −O, and −OH exposed on $Ti_3C_2T_x$ flakes. Figure 1B displays the XRD patterns of Ti_3AlC_2 and $Ti_3C_2T_x$. Peaks at 41.8, 38.9, 38.7, 34.0, 19.0, and 9.4° can be assigned to the (105), (104), (103), (101), (004), and (002) crystal planes of Ti_3AlC_2, respectively.[4] After etching and delamination process, the strong peak of Al(104) completely disappeared, indicating the Al atom is successfully removed from the MAX phase.[11] Interestingly, the (002) crystal plane of MXene shifts to a lower position of 6.15°, evidencing the increase in layer spacing after etching and ultrasonic exfoliation, indicating the successful synthesis of single-layered MXene. The freeze-dried $Ti_3C_2T_x$ exhibits poor formability with products in the form of fluffy powder (inset of Figure 1B), which can be easily dispersed in DI water under mild sonication. As also displayed in Figure 1C,D, the prepared MXene flake shows a well-defined 2D configuration with a size of about 1000 nm and a thickness of 2.64 nm, confirming the successful fabrication of monolayer $Ti_3C_2T_x$ nanosheets.[12]

Because PINFs are highly hydrophobic and difficult to be processed in water, the as-spun hydrophilic PAANFs prior to imidization are selected as building blocks to prepare MXene aerogels. Here, PAA spinning solution with a suitable concentration is prepared through the polycondensation reaction of ODA and PMDA monomers; through electrospinning and high-speed homogenizing treatment to shear and disperse the PAANF films (Figure S1A), short PAANFs with a length of 20−50 μm and a diameter of ∼500 nm were obtained (Figure S1B,C). Interestingly, freeze-dried PINFs display better 3D formability than MXene due to the random weaving and entangling of short PINFs (Figure S2). MXene flakes and PAANFs were assembled in water under mild magnetic stirring to obtain a homogeneous PAANF/MXene mixture, which was subjected to freeze-drying and thermal imidization to obtain PINF/MA composite aerogel. As demonstrated in the upper right corner of Figure 1A, the as-assembled lightweight PINF/MA aerogel can steadily stand on a dandelion. Obviously, PINFs can act as cross-linking agents to help improve the 3D formability of MXene flakes.

Figure 2A displays the XRD patterns of PAANFs, PINFs, MXene, and PINF/MA. It is obvious that the polymeric PINFs show an amorphous diffraction peak at around 20° after imidization, which can be attributed to the dehydration cyclization of the PAANF precursor after heat treatment at 300 °C. PINF/MA shows a sharp peak at about 6.3° with weakened peak intensity, demonstrating that the crystalline structure of MXene is significantly affected by the incorporation of PINFs. Furthermore, the (002) characteristic peak of MXene shifts from 6.71 to 6.21° in the XRD pattern of PINF/MA, which is ascribed to the expansion of MXene layers by the intercalation of PINFs.[8] Raman characterization was performed to investigate the structure of the composites (Figure 2B). Two peaks of PINFs at 1376 and 1612 cm^{-1} can be readily indexed to the C−N stretching of the imide ring and the vibrations of aromatic imide ring, respectively.[16] The characteristic peaks of MXene at 1377 and 1559 cm^{-1} are attributed to the C−C vibrations.[17] Especially, the Raman spectrum of MXene shows several peaks between 100 and 800 cm^{-1};[18] the A_{1g} peak at 699 and 149 cm^{-1} can be readily indexed to the symmetric out-of-plane vibrations of C and Ti, while the E_g in-plane shear vibrations of the surface functional groups, C, and Ti correspond to the peaks at 604, 396, and 269 cm^{-1}, respectively.[5] The Raman spectrum of the PINF/MA composite exhibits the D and G peaks of PINFs at 1337 and 1580 cm^{-1}, coupled with the Ti/C vibrational peaks of MXene, proving the integration of two building blocks. It is noteworthy that the I_D/I_G value of MXene decreased significantly from 1.56 to 1.19 after its assembly with PINFs, demonstrating the expanded layer spacing of MXene stemmed from the intercalation of short nanofibers and thus helps to prevent the self-stacking and rapid oxidation of MXene flakes.[19]

XPS measurement was also utilized to investigate the composition and chemical bonding of the prepared PINF/MA composite aerogel. Survey spectra in Figure 2C help to identify the C, N, O, Ti, and F atoms in PINF/MA derived from the polymeric polyimide and inorganic MXene. Compared with the C 1s spectra of MXene and PINFs presented in Figure S3A,B, the O−C═O, C−O, C−C, and Ti−C−O peak intensities in C 1s spectra of PINF/MA have significantly increased (Figure 2D); the C−Ti peak intensity decreases on the contrary, plus a new C−Ti−N peak appeared, confirming the intimate chemical interaction between PINFs and MXene building blocks.[20,21] Figures 2E and S4 show the Ti 2p spectra of PINF/MA and MXene, respectively. All the Ti $2p_{3/2}$ and Ti $2p_{1/2}$ peaks in the spectrum of PINF/MXene composites are almost identical to those of pure MXene. Above XPS results evidencing the incorporation of PINFs can not only prevent the MXene flakes from restacking but also protect them from potential oxidation during the freeze-drying and thermal imidization process.[6] A systematic FT-IR study on polymer nanofibers, MXene, and their composites is further conducted with results presented in Figure 2F,G. The absorption peaks of PAANFs at 1498 cm^{-1} (C═C stretching vibration on the benzene ring), 1539 cm^{-1} (C−N(H)−C), 1650 cm^{-1} (C═O), 3055 cm^{-1} (−OH), and 3261 cm^{-1} (N−H) can be clearly observed;[20,22] after heat treatment below 300 °C, the N−H and −OH peaks vanish and are replaced with the new absorption peaks of C═O (1770, 1703 cm^{-1}) and C−N (1363 cm^{-1}), indicating the successful thermal imidization of PAANFs to PINFs.[6] The FT-IR spectrum of pure MXene shows characteristic peaks at 3493, 1642, and 667 cm^{-1}, in accordance with the stretching vibrations of O−H, C−O, and Ti−O, respectively (Figure 2G).[9] After the synergistic assembly of PAANFs and MXene and thermal imidization to obtain PINF/MA composite aerogel, the peak intensity at 3493, 1642, and 667 cm^{-1} drops sharply; more interestingly, the absorption peaks of C═O, C−N, and C═C manifest the clear shift to lower wavenumbers. All these changes are caused by the intimate hydrogen bonding between the surface-active −OH groups on MXene flakes and the ═O/−NH groups on PINFs (as schematically illustrated in Figure 2H). The strong interfacial bonding between two building blocks ensures the efficient assembly of PINFs and MXene and the final formation of a lightweight and robust PINF/MXene aerogel.

In addition, the thermal stability of MXene, PAANFs, PINFs, and PINF/MA composite aerogels was investigated through TGA. As can be seen in Figure 2I, the thermal

https://doi.org/10.1021/acsami.1c13863
ACS Appl. Mater. Interfaces 2021, 13, 47134−47146

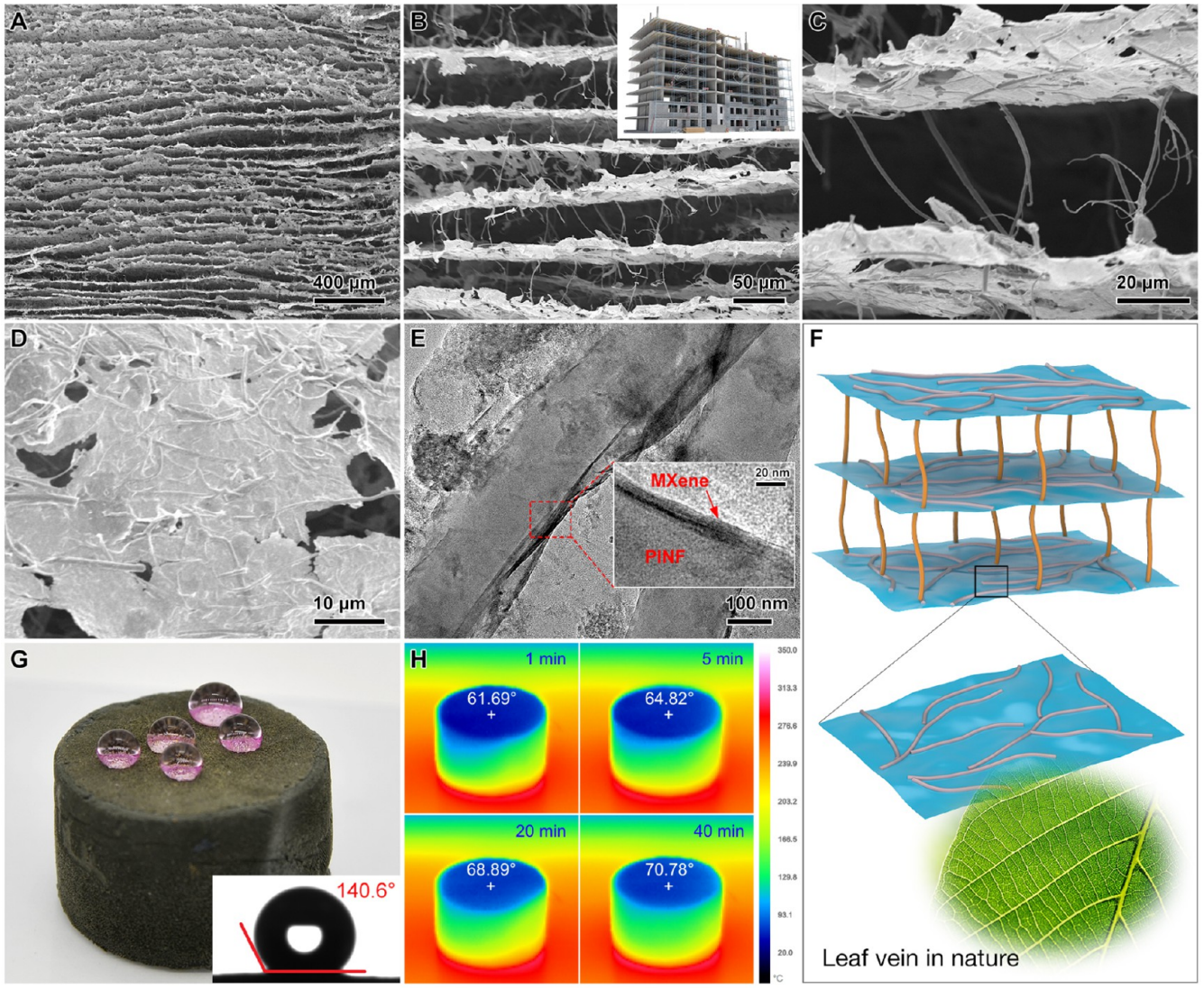

Figure 3. (A–D) SEM images of PINF/MA composite aerogel. (E) TEM images focused on the leaf vein-like lamellar structure. (F) Schematic showing the 3D "lamella-pillar" microporous architecture and the leaf vein-like lamellar structure in PINF/MA composite aerogel. (G) Digital photograph of water droplets on the PINF/MA surface. The inset shows the corresponding water contact angle. (H) Infrared thermal images of the PINF/MA composite aerogel at a heating stage (300 °C) captured at different times.

decomposition process of the above materials can be divided into three stages: (1) the evaporation of adsorbed water and residual solvent causes a slight weight decrease below 100 °C, (2) large mass loss between 100–560 °C due to the decomposition of surface groups on polymer nanofibers (−OH, −COOH, and −NH), and (3) massive weight loss at high temperature (>560 °C) caused by the thermal decomposition of polymeric PAANFs and PINFs. Compared with PAANFs, the initial decomposition temperature of PINFs ($T_{5wt\ \%}$, the temperature at 5% weight loss) is raised from 104 to 251 °C because of the improved thermal stability of polyimide after imidization. The weight loss of MXene mainly originated from the dehydration reaction (Ti−OH + Ti−OH → H_2O + Ti−O−Ti)[23] and thus explains its little mass change at high temperature and under a nitrogen atmosphere (84.6 wt %). Interestingly, PINF/MA composite aerogel exhibits the highest initial decomposition temperature (about 300 °C) and maximum decomposition rate temperature (T_{max} is about 550 °C) compared to those of pure PAANFs, PINFs, and MXene, which stems from the good thermal stability of PINFs. Besides, 3D macroporous structures within PINF/MA composite aerogel may result in the discontinuity of heat conduction and thus significantly improve the thermal stability of the PINF/MA. In consequence, the maximum weight loss of PINF/MA is largely reduced with respect to the other samples.

Figure 3 shows the morphologies of the PINF/MA composite aerogel prepared with the PAANF: MXene mass ratio of 1:1. The SEM image under low magnification displays that PINF/MA is constructed from 3D interconnected networks with orderly aligned lamella layers (Figure 3A). The formed 3D microporous structures possess extraordinary porosity with short PI nanofibers acting as the support pillars between adjacent thin layers similar to the function of steel bars in building structures (inset of Figure 3B), which ensures spring-like flexibility and bendability (Figure 3B,C). The height between two parallel layers is in a range of 20–50 μm, so there is enough space for the aerogel to cope with the deformation during the compression process while maintaining a low density. A further close observation on the lamella layers under high magnification reveals that PINFs and MXene are

https://doi.org/10.1021/acsami.1c13863
ACS Appl. Mater. Interfaces 2021, 13, 47134–47146

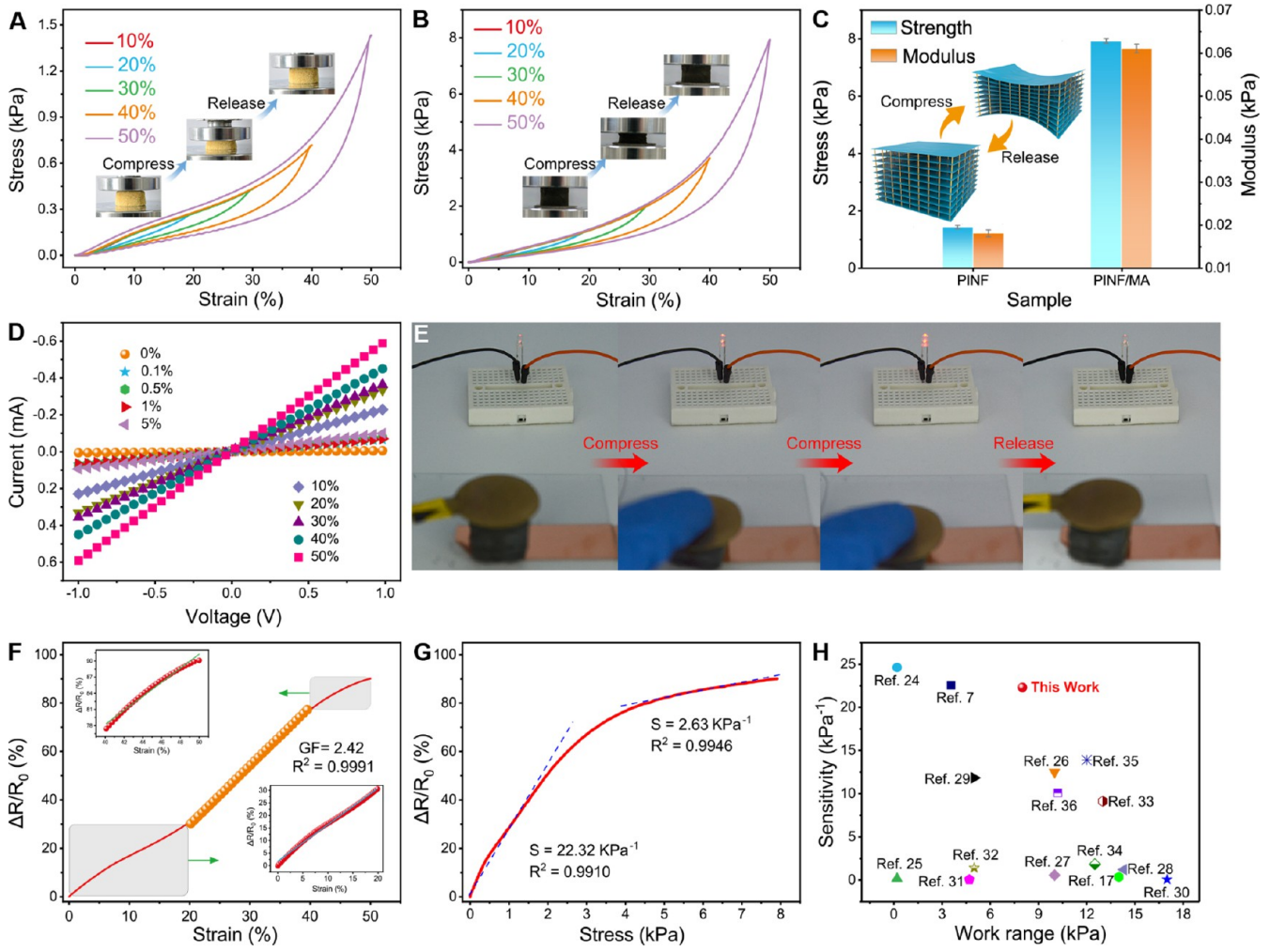

Figure 4. Stress−strain curves of (A) PINF aerogel and (B) PINF/MA composite aerogel under various strains. Insets showing the corresponding digital photographs of compression-release processes. (C) Comparison of the compressive modulus and strength between PINF/MA composite aerogel and PINF aerogel. (D) *I*−*V* curves of PINF/MA under different strains. (E) Demonstration showing the change in electrical conductivity of PINF/MA composite aerogel during compression-release. $\Delta R/R_0$ of PINF/MA as a function of (F) compression strain and (G) compression stress. (H) Comparison of the sensitivity and sensing range between PINF/MA composite aerogel and previously reported strain sensors.

cross-linked to form a leaf vein-like lamellar structure (Figure 3D), where PINFs act as attachment points for the connection of MXene flakes through the strong interfacial interaction. These interesting lamella layers are formed under the direction and extrusion of ice crystals during the freeze-drying process. The TEM image of the lamellar structure discloses the intimate interaction between nanofibers and 2D MXene flakes so that the few-layered $Ti_3C_2T_x$ nanosheets are tightly wrapped on PINFs through the strong interfacial bonding during the sol−gel process (Figure 3E), thus laying a solid foundation for the mechanical and electrical properties of the composite aerogel. The elemental mapping of the selected area also displays that C, O, N, and Ti are clearly distributed on the leaf vein-like lamellar structure (Figure S5). Such a vascular-like structure not only inhibits the excessive self-stacking of MXene flakes but also bridges the small MXene flakes to construct an integrated conductive path, thereby enhancing the mechanical property and electrical conductivity of the composite aerogel simultaneously. The unique 3D "lamella-pillar" microporous architecture of PINF/MA composite aerogel is also schematically illustrated in Figure 3F.

The as-prepared PINF/MA composite aerogel also exhibits the super-hydrophobic property. As demonstrated in Figure 3G, colored water droplets can steadily stay on the aerogel instead of penetrating it, resulting in the water contact angles of 140.6° (inset of Figure 3G). The hydrophobicity of the composite aerogel mainly comes from two aspects. First, the intrinsic hydrophobicity of PINF building blocks can render the composite aerogel with water-proof capability; assembled porous 3D monolith with micron-level roughness can further reduce the water−solid contact area, thereby greatly enhancing the hydrophobic property of the PINF/MA composite aerogel. In addition, the heat insulation performance is also assessed using an infrared thermal imaging camera. The surface temperature of PINF/MA (thickness = 15 mm) heated on a 300 °C platform slowly rises as displayed in Figure 3H, which reaches only 70.78 °C after being heated for 40 min, nearly 1/4 of the hot stage temperature, implying the long-term thermal insulating stability of PINF/MA composite aerogel. Besides, the thermal conductivity of PINF/MA composite aerogel at 300 °C is measured to be 90.5 mW m^{-1} K^{-1}. The low density and high porosity of the PINF/MA composite aerogel significantly decrease its thermal conductivity in the solid

https://doi.org/10.1021/acsami.1c13863
ACS Appl. Mater. Interfaces 2021, 13, 47134−47146

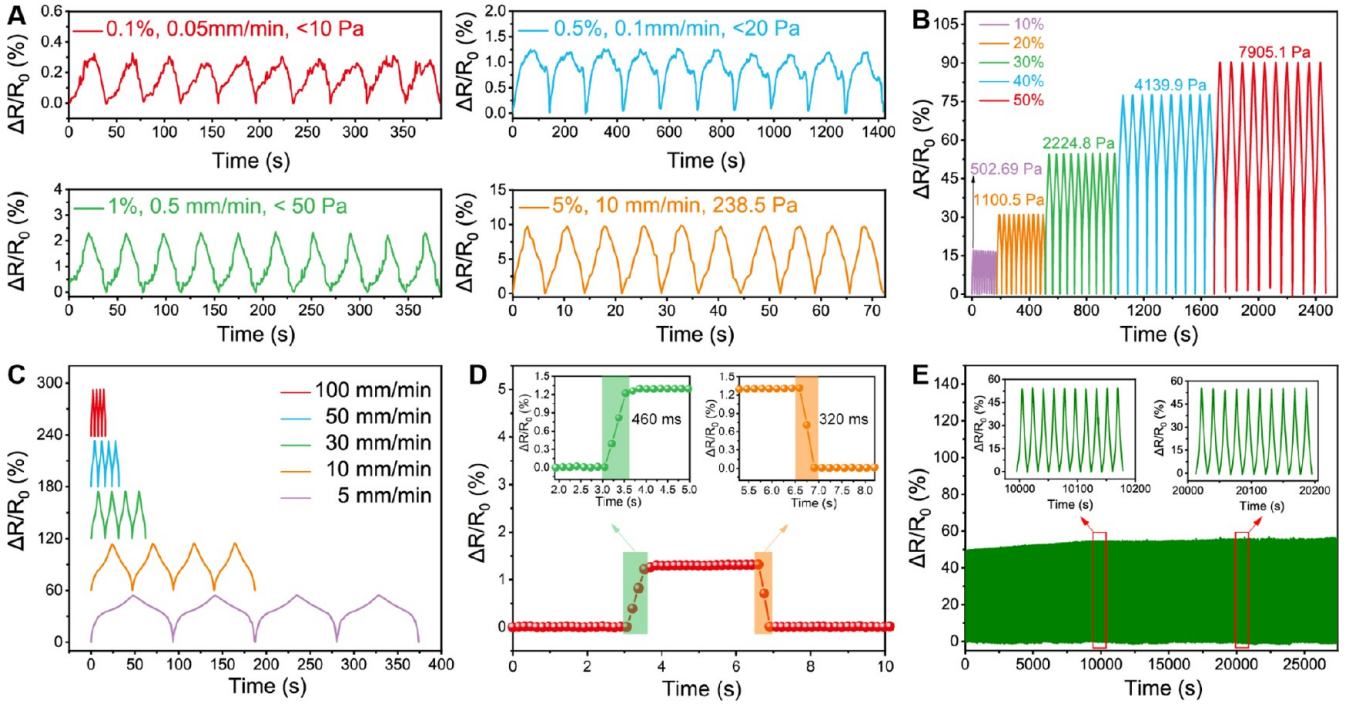

Figure 5. (A,B) multi-cycle response curves of the PINF/MA strain sensor under various compressive strains. (C) $\Delta R/R_0$ of the PINF/MA at various compression rates under 30% strain. (D) Response/recover times of the PINF/MA at a compression rate of 500 mm min^{-1} under 0.5% strain. (E) Long-term stability performance of the PINF/MA strain sensor at a compression rate of 10 mm min^{-1} and under a compression strain of 30% for 30,000 s (insets are the enlarged parts of 9995−10,179 and 20,012−20,195 s).

phase, and the parallelly distributed hierarchical structure in the aerogel further reduces the radiant heat transfer; the two factors collaboratively enhance the thermal insulation performance of PINF/MA composite aerogel. Hence, the good thermal insulation properties and strong hydrophobicity of the PINF/MA composite aerogel can ensure its stability and versatility in harsh environments.

Generally, good mechanical properties are essential for a piezoresistive sensor. Figure 4A,C indicates that PINF aerogel can only withstand relatively small stress (maximum stress of 1.42 kPa at a strain of 50%) and displays low modulus, which may stem from the poor interconnection between building blocks. In contrast, the stress of PINF/MA at 50% compressive strain (8 kPa) is much higher than that of PINF aerogel (Figure 4B). Specifically, two different stages can be identified during the compression of PINF/MA at all strains. The first part is a linear elastic region below 40% strain, where the stress increases slowly due to the initial compression of the macroporous structure, followed by a sharp increase in stress at higher strain (ε > 40%) due to the collision between adjacent parallel layers. Notably, the PINF/MA can still restore its original shape after a cyclic compression-release (see the inset in Figure 4B). Video S1 further proves the excellent mechanical flexibility and resilience of PINF/MA composite aerogel. The inset of Figure 4C schematically shows the compression and rebound process of the PINF/MA composite aerogel. PINFs between the robust leaf vein-like lamella layers can serve as supporting scaffolds in adjacent layers like pillars to enhance the structural stability of PINF/MA; the formed macropores in PINF/MA aerogel contract perpendicular to the compression direction upon the force loading, leading to the large compression of the composite aerogel. Once the force is released, the internal porosity of PINF/MA can completely restore to its original state without causing structural fatigue due to the high elasticity of the pore wall and PINF pillars. Hence, the combination of MXene flakes and PINFs can help enhance the mechanical strength of the composite aerogel.

The real-time current response curves ($I-V$ curves) under various strains were measured to explore the linear response performance of aerogel. As shown in Figure 4D, the $I-V$ curve of PINF/MA shows good linearity under different strains and the slope of the $I-V$ curve increases along the strain due to the decrease in resistance under compression, which is caused by the increased contact surface and enhanced conductive paths between conductive lamella layers. Figure 4E and Video S2 vividly display that the resistance change of PINF/MA composite aerogel upon compression and release can be reflected by the brightness of the connected LED bulb, showing the promising applications of the composite aerogel in highly sensitive pressure sensors. Besides, the exact volumetric conductivity of the PINF/MA composite aerogel was measured to be 0.038 S m^{-1}. Figure 4F presents the relative resistance change of PINF/MA in a strain range of 0−50% ($\Delta R/R_0 = (R_0 - R_t)/R_0$, where R_0 and R_t are the initial resistance and resistance when pressure is applied, respectively). It is obvious that the resistance change of PINF/MA in the entire compression process consists of three linear parts. When the compressive strain range is 0−20%, the increase in resistance is relatively slow due to the gradual formation of a conduction path upon small compression, in accordance with the results in Figure 4B. When the PINF/MA composite aerogel is further compressed to the strain of 40%, its resistance change exhibits a significantly increased slope, attributing to the enhanced charge transfer from the face-to-face contact of the parallel-layered structure. As the distance approaches further, the conduction area inside the composite aerogel increases and the number of conduction paths increases; hence, the resistance shows a rapid linear decline.

https://doi.org/10.1021/acsami.1c13863
ACS Appl. Mater. Interfaces 2021, 13, 47134−47146

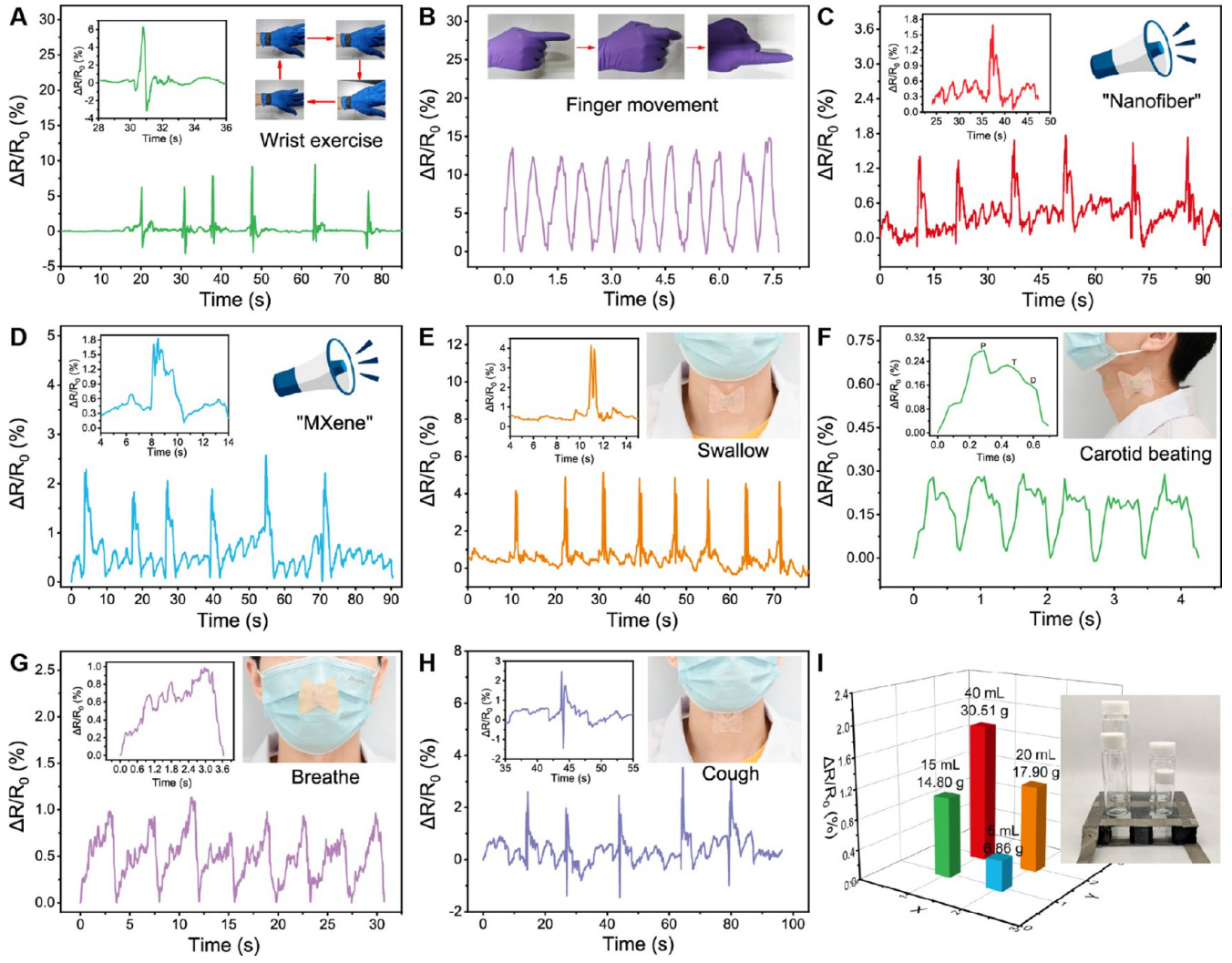

Figure 6. Application of the PINF/MA strain sensor for the real-time monitoring of different human activities: large motion signals of (A) wrist and (B) finger bending. Small motion signals of (C,D) different words pronunciation, (E) swallowing, (F) carotid beating, (G) breathing, and (H) coughing. (I) Photograph of the assembled PINF/MA sensor array (3 × 3 pixel) and the corresponding pressure distribution map when different vials are placed on the sensor array.

sFinally, the PINF/MA composite aerogel enters the densification area under large compression strain and the parallel-layered structures begin to stack on each other, leading to a slow increase in conductivity. The resistance change of PINF/MA composite aerogel versus the applied stress was also studied. Identical to Figure 4B, the pressure sensitivity curve also shows two obvious linear regions as the applied pressure increases (Figure 4G). To start with, $\Delta R/R_0$ increases sharply in a linear pressure range of 0−3 kPa, giving a sensitivity (S) as high as 22.32 kPa^{-1}. When the exerted stress is beyond 3 kPa, the S value is reduced to 2.63 kPa^{-1} due to the internal densification of PINF/MA as already explained in Figure 4B,F. A detailed comparison of the pressure sensitivity and working range between PINF/MA and previously reported piezoresistive sensors is given in the plot of Figure 4H.[7,17,24−36] Excitingly, PINF/MA composite aerogel with unique 3D "lamella-pillar" microporous architecture manifests the well-balanced sensing performance in terms of a superior pressure sensitivity (22.32 kPa^{-1}) and a wide working range (8 kPa). It is envisioned that PINF/MA composite aerogels may have great application prospects in the field of flexible piezoresistive sensors.

Figure 5A,B shows the cyclic response performance of PINF/MA under various compressive strains, where stable and reproducible signals can be output in a wide strain range from 0.1 to 50%. Specifically, a subtle deformation of 0.1% with generated stress lower than 10 Pa can be accurately sensed using an aerogel sensor, demonstrating the ultra-low detection limit and extraordinary stability of PINF/MA. Meanwhile, the PINF/MA pressure sensor is also able to detect large deformation of 50% strain; all the cyclic resistance curves display highly stable and repeatable signals, which may originate from the orderly constructed lamellar configuration of the composite aerogel. Interestingly, the PINF/MA strain sensor undergoes a fast resistance change in the entire small deformation range of 0.1−5%, while this trend tends to slow down as the applied strain increases to a relatively higher region of 10−50% (Figure 6B), in accordance with the two linear regions as displayed in Figure 4G. The above results identify the remarkable ability of PINF/MA in the detection of both small and large deformations. Furthermore, the resistance change of the strain sensor at various compression speeds under the strain of 30% was investigated. As shown in Figure 5C, the higher the compression rate is, the shorter the time

https://doi.org/10.1021/acsami.1c13863
ACS Appl. Mater. Interfaces 2021, 13, 47134−47146

taken for PINF/MA to complete a compression−release cycle. It should be noted that the maximum resistance change is not affected by the strain rate, demonstrating the stable conductive path derived from the integrated 3D "lamella-pillar" microporous architecture. The response/recover times of the pressure sensors are also important indexes to appraise their sensing performance. Under an instantaneous strain of 0.5% at a compressing rate of 500 mm min^{-1}, the PINF/MA sensor exhibits a fast response time of 482 ms coupled with a recovery time of 321 ms. The recovery time depends on the speed at which it can elastically return to its original shape once the external pressure is removed. The short recovery time implies the excellent resilience, stable internal structure, and high mechanical properties of PINF/MA composite aerogel. Cycle life is another essential parameter that determines the practical application value of pressure sensors. Hence, the durability of the piezoresistive behavior of the PINF/MA strain sensor was evaluated under the strain of 30% at a compressing rate of 10 mm min^{-1}. As shown in Figure 5E, there rarely exists any resistance decrease for the PINF/MA aerogel sensor even after 1500 compression cycles, and the resistance change rate also showed a quite good repeatability and good stability (insets of Figure 5E). Besides, the stress−strain curves of the PINF/MA strain sensor at each compression cycles almost stay unchanged (Figure S6). The above results display the high sensitivity, low detection limit, great repeatability, and good durability of the PINF/MA piezoresistive sensor.

Considering its good mechanical properties and piezoresistive sensing characteristics, the prepared PINF/MA composite aerogel can be used as flexible/wearable sensors to detect human motions in real time by attaching the assembled sensor (Figure S7) to the human body. As shown in Figure 6A,B, the cyclic bending activity of the wrist and finger can be real-timely monitored using an attached pressure sensor on the joints. Because the pressure sensor undergoes compression deformation during the bending of joints, the $\Delta R/R_0$ witnessed a sharp increase and recovers to the initial state when the wrist/finger is straightened. The sharp on−off peaks detected using the PINF/MA pressure sensor indicate its fast response and high sensitivity. Detection capability toward small motion signals was further investigated in detail. As depicted in Figure 6C,D, the resistance change curves acquired by fixing the pressure sensor on the throat show obvious characteristic peaks when the tester utters words such as "MXene" and "Nanofiber", which are mainly due to the complex muscles and vocal cord vibration during the pronunciation process, revealing the potential voice recognition applications of PINF/MA aerogel sensors. Besides, the flexible sensor is also able to monitor the swallowing movements in real time. Typically, there are two typical peaks in the detected swallowing signal, corresponding to the contraction and extension of the throat during the swallowing and recovering process, respectively (Figure 6E). Furthermore, the real-time monitoring of the carotid artery pulsation signal is presented in Figure 6F, which shows a waveform with 79 pulsations per min. It is obvious that the detected signal shows three distinguishable characteristic peaks of carotid artery pressure, P, T, and D (inset of Figure 6F).[36] Notably, the relative resistance produced by the carotid artery pulsing is very small (<0.3%), verifying the remarkable sensitivity of the flexible pressure sensor. In addition, the sensor fixed on a surgical mask also outputs a stable and regular signal of breathing (Figure 6G), which may provide a simple, low-cost, and efficient method for long-term breath detection in human health monitoring. Apart from these, the aerogel sensor was also used to test the signal changes of coughing with characteristic peaks appearing in Figure 6H. To further explore the practical applications of the pressure sensor, an arrayed sensor in 3 × 3 configuration was assembled with the PINF/MA composite aerogel. When four vials with different sizes/masses are placed on the sensor array, the pressure distributions and the positions of the vials can be mapped in the matrix (Figure 6I). In summary, the flexible pressure sensor based on PINF/MA aerogel reveals exceptional capabilities in the real-time detection of tiny and large human movements, which definitely possesses great potential in health monitoring and human−machine interface applications.

The 3D "lamella-pillar" microporous architecture composed of conductive and parallelly arranged layered structure provides PINF/MA composite aerogel with tremendous prospects in EMA. Generally, the EMA performance mainly depends on the relative complex permittivity ($\varepsilon_r = \varepsilon' - j\varepsilon''$) and complex permeability ($\mu_r = \mu' - j\mu''$) of a material.[37] Figures S8 and S9 respectively show the real part (ε' and μ'), imaginary part (ε'' and μ''), and loss tangent ($\tan \delta_\varepsilon = \varepsilon''/\varepsilon'$ and $\tan \delta_\mu = \mu''/\mu'$) of the complex permittivity and complex permeability of the PINFs and PINF/MA composite aerogels in a frequency range of 0.5−18 GHz. As well known that the real part (ε'' and μ'') of the complex permittivity and the complex permeability respectively represents the storage capacity of electrical energy and magnetic energy, and the imaginary part (ε' and μ') represents the loss capacity of electrical energy and magnetic energy.[38] Both MXene and PINFs are non-magnetic materials; hence, the real part of the permeability of the composite aerogel is close to 1, and the imaginary part is close to 0 (Figure S8), and thus, their permeability can be ignored.

Because PINFs are not conductive, their dielectric constant is high and dielectric loss is low, thus resulting in the poor dielectric loss capability. As shown in Figure S9A,B, PINF aerogel exhibits negligible EMA performance with ε' nearly zero and ε'' remains at 2.2 in a frequency range of 0.5−18 GHz. Contrarily, the ε' value of PINF/MA dropped from a high value of 9.1 to 3.1, which can be explained by the increase in the polarization hysteresis.[39] It is widely acknowledged that the resonance behavior of dielectric materials largely depends on the ion polarization, interfacial polarization, electronic polarization, dipolarization, and space charge polarization.[40,41] In this case, the increase in ε'' for the composite aerogel is mainly attributed to the enhancement of dipolar polarization caused by the functional groups and defects of the $Ti_3C_2T_x$ sheet and the interfacial polarization between the dipoles. Hence, MXene can effectively increase the consumption ability of composite aerogel toward electromagnetic waves. Besides, EMA materials with high dielectric loss tangent ($\tan \delta_\varepsilon$) values can effectively absorb and convert microwaves into other types of energy. The $\tan \delta_\varepsilon$ of PINF/MA increases significantly in the frequency range of 0.5−18 GHz (Figure S9C), implying that the incorporation of MXene can effectively consume electromagnetic energy and significantly increase the attenuation of electromagnetic waves. The above dielectric properties can be explained by Debye theory in eq 1.[18]

$$\left(\varepsilon' - \frac{\varepsilon_s + \varepsilon_\infty}{2}\right)^2 + (\varepsilon'')^2 = \left(\frac{\varepsilon_s - \varepsilon_\infty}{2}\right)^2 \quad (1)$$

https://doi.org/10.1021/acsami.1c13863
ACS Appl. Mater. Interfaces 2021, 13, 47134−47146

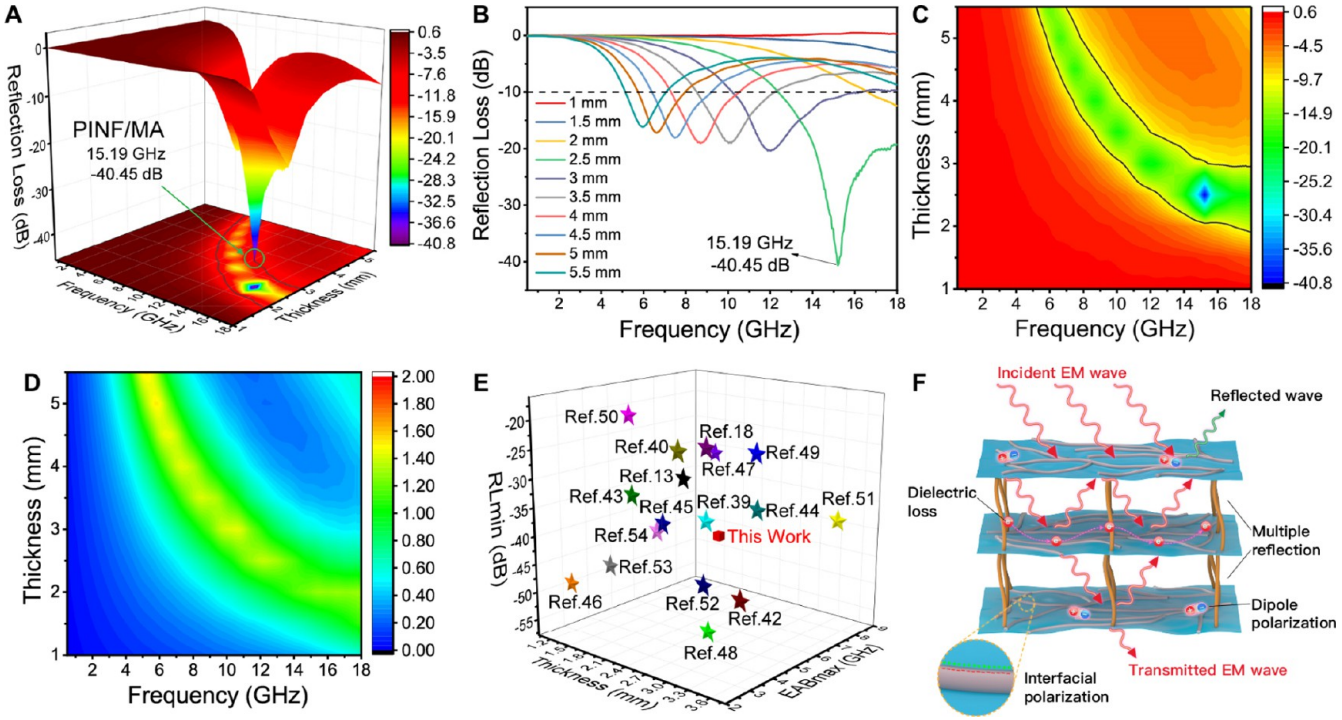

Figure 7. (A,B) 3D RL map and 2D RL curves of PINF/MA composite aerogel. (C) Frequency dependence of RL of PINF/MA composite aerogel. (D) 2D impedance matching contour map ($|Z_{in}/Z_0|$) of PINF/MA composite aerogel. (E) Comparison of the EMA performance between PINF/MA composite aerogel and related materials. (F) Schematic illumination of the EM wave dissipation mechanism for PINF/MA composite aerogel.

where ε_s is the static dielectric constant and ε_∞ denotes the dielectric constant at infinite frequency. When the graph of ε' and ε'' is a single semicircle (Cole−Cole semicircle), it may correlate with a Debye relaxation process involving the dielectric polarization effect. Apparently, the Cole−Cole plot of PINF/MA shows multiple semicircles (Figure S10), ascribing to the multiple polarization relaxations in the composite aerogel (depolarization, dielectric polarization, interface polarization, etc.). Additionally, the conductivity loss is also indicated by the emergence of the tail in the Cole−Cole semi-circle of PINF/MA, which is mainly due to the good electrical conductivity of the composite aerogel.

To investigate the EMA performance of the PINF/MA composite aerogel in detail, the reflection loss (RL) of incident electromagnetic wave was calculated according to the following eq 2[42]

$$\mathrm{RL\ (dB)} = 20 \lg \left| \frac{Z_{in} - Z_0}{Z_{in} + Z_0} \right| \tag{2}$$

where Z_0 is the impedance of the free space and Z_{in} is the input impedance expressed as[43]

$$Z_{in} = Z_0 \sqrt{\frac{\mu_r}{\varepsilon_r}} \tanh\left[j \left(\frac{2\pi f d}{c} \right) \sqrt{\mu_r \varepsilon_r} \right] \tag{3}$$

where μ_r and ε_r are the relative permeability and permittivity of the composites, f represents the frequency of the electromagnetic wave, j denotes the imaginary unit, c stands for the velocity of light in free space, and d is the thickness of the sample. Herein, the real and imaginary parts of μ_r are 1 and 0, respectively, due to the weak magnetism of the aerogel. In general, the −10 dB absorbing bandwidth (90% absorption) is one of the most important criteria to evaluate the EMA performance.[44] It is no doubt that PINFs possess poor MA performance throughout the frequency range due to the lowest complex permittivity and dielectric loss tangent (Figure S11). By contrast, the EMA performance of the PINF/MA composite aerogel is greatly improved, owing to the introduction of conductive 2D MXene flakes. As shown in Figure 7A, PINF/MA manifests a minimum RL value (RL_{min}) of −40.45 dB when the thickness is 2.5 mm at a frequency of 15.19 GHz. Its effective absorption bandwidth (EBA, RL < −10 dB) is 5.66 GHz (12.34−18 GHz), covering the entire Ku-band (Figure 7B,C). Besides, PINF/MA exhibits the largest absorption bandwidth of 6.07 GHz (10.24−16.31 GHz) when the thickness is 3 mm; the minimum RL in this case is 20.47 dB at 12.01 GHz.

To better understand the EMA properties of PINF/MA composite aerogels, their impedance matching degree is thoroughly investigated. Typically, the impedance matching degree of an EMA material should be equal or close to that of the free space,[45] which can be evaluated by the normalized characteristic impedance calculated as $Z = |Z_{in}/Z_0|$.[46] The 2D impedance gradient contour maps of PINFs and PINF/MA versus sample thickness and measuring frequency are presented in Figures 7D and S11D. The green color region is the area in which $Z = 1$, an indication of perfect impedance matching. Because PINFs are electrically insulating and there is no other substance that can effectively dissipate electromagnetic waves, nearly all the electromagnetic waves directly pass into the air, and there is almost no RL. Figure S11D shows that the impedance matching value of PINFs is far greater than 1 in the entire test frequency range. In contrast, Figure 7D reveals that the impedance matching of PINF/MA is close to 1 in a frequency range of 6−18 GHz, suggesting that MXene can effectively increase the conductivity of the

https://doi.org/10.1021/acsami.1c13863
ACS Appl. Mater. Interfaces 2021, 13, 47134−47146

composite aerogel, thereby improving its impedance matching. Good impedance matching means that more incident electromagnetic waves can be guided into the interior of the composite aerogel, thus laying a foundation for the interface polarization, multiple reflections, and conductance losses inside the parallelly aligned lamellar structures. Meanwhile, the attenuation constant is also calculated using eq 4 to assess the electromagnetic energy attenuation ability of PINF/MA composite aerogel.[47]

$$\alpha = \frac{\sqrt{2}\pi f}{c} \sqrt{(\mu''\varepsilon'' - \mu'\varepsilon') + \sqrt{(\mu''\varepsilon'' - \mu'\varepsilon')^2 + (\mu''\varepsilon' + \mu'\varepsilon'')^2}} \quad (4)$$

As shown in Figure S12, as the frequency increases, the EM attenuation constant of PINF/MA composite aerogel presents a steadily ascending trend, which is helpful to increase the attenuation of incident electromagnetic waves. Finally, the PINF/MA composite aerogel is also competitive among other macroporous microwave absorbing materials (Figure 7E).[13,18,39,40,42−54]

Figure 7F illustrates the mechanism of EM wave dissipation in PINF/MA composite aerogel. First of all, the intercalation of PINFs in MXene flakes can neutralize the high conductivity of MXene caused by restacking, thereby improving the impedance matching of the composite aerogel and promoting more EM waves to enter the interior space. Subsequently, the entered EM waves can undergo multiple internal reflections and scattering between the parallel hierarchical structure constructed with vein-like PINF/MXene lamella layers so that the EMA performance of the composite aerogel is significantly improved. At the same time, the 3D interconnected PINF/MA networks are beneficial for the construction of a continuous conductive pathway, which facilitates the dielectric loss to transform electromagnetic waves into electricity and/or heat along the 3D network. In addition, the active edges of MXene flakes and the strongly bonded PINF/MXene interface can act as polarization centers to promote the formation of dipole polarization and interfacial polarization, which are also conducive for the absorption of electromagnetic waves.

4. CONCLUSIONS

In summary, a multi-functional PINF/MA composite aerogel with unique 3D "lamella-pillar" microporous architectures is constructed via the synergistic assembly of short PINFs and MXene flakes based on the strong interfacial bonding between both building blocks. The leaf vein-like lamella layers composed of few-layered $Ti_3C_2T_x$ and embedded PINFs can provide superior mechanical stability and decent electrical conductivity, which are parallelly aligned and intercalated by robust PINF "pillars", resulting in the remarkable mechanical properties of the composite aerogel. Benefitting from the intriguing structural advantages, the constructed PINF/MA composite aerogel exhibits remarkable piezoresistive sensing performance in terms of a wide pressure range of 0−8 kPa (50% strain), excellent linear sensitivity (22.32 kPa^{-1}), an ultra-low detection limit (0.1% strain and <10 Pa), and excellent compression and rebound stability (1500 cycles). Additionally, the PINF/MA composite aerogel is capable of detecting various human motions (including carotid artery beating, vocal cord vibration, and different joint movements). By virtue of the good conductivity of the vein-like lamella layers, PINF/MA composite aerogel also manifests excellent electromagnetic wave absorption performance with RL_{min} reaching −40.45 dB at 15.19 GHz, along with an EAB of 5.66 GHz (12.34−18 GHz). The outstanding mechanical properties and excellent sensing and EMA performance make PINF/MA composite aerogel a promising candidate in flexible/wearable piezoresistive sensors and microwave absorbers.

■ ASSOCIATED CONTENT

Supporting Information

The Supporting Information is available free of charge at https://pubs.acs.org/doi/10.1021/acsami.1c13863.

Digital photograph and SEM images of homogeneous PAANF dispersion and PINF aerogel; XPS spectra of MXene and PINFs; elemental mapping of PINF/MA composite aerogel; supplementary permittivity, permeability, Cole−Cole semicircle curve of the samples; comprehensive EMA performance of PINF aerogel; and attenuation constants of different aerogels (PDF)

Mechanical flexibility and resilience of PINF/MA composite aerogel (MP4)

Resistance change of PINF/MA composite aerogel (MP4)

■ AUTHOR INFORMATION

Corresponding Authors

Yunpeng Huang − *Key Laboratory of Synthetic and Biological Colloids, Ministry of Education, School of Chemical and Material Engineering, Jiangnan University, Wuxi 214122, China*; orcid.org/0000-0002-8710-9062; Email: hypjnu@jiangnan.edu.cn

Tianxi Liu − *Key Laboratory of Synthetic and Biological Colloids, Ministry of Education, School of Chemical and Material Engineering, Jiangnan University, Wuxi 214122, China*; Email: txliu@jiangnan.edu.cn

Authors

Lei Pu − *Key Laboratory of Synthetic and Biological Colloids, Ministry of Education, School of Chemical and Material Engineering, Jiangnan University, Wuxi 214122, China*

Yongpeng Liu − *Key Laboratory of Synthetic and Biological Colloids, Ministry of Education, School of Chemical and Material Engineering, Jiangnan University, Wuxi 214122, China*

Le Li − *Key Laboratory of Synthetic and Biological Colloids, Ministry of Education, School of Chemical and Material Engineering, Jiangnan University, Wuxi 214122, China*

Chao Zhang − *State Key Laboratory for Modification of Chemical Fibers and Polymer Materials, College of Materials Science and Engineering, Donghua University, Shanghai 201620, China*; orcid.org/0000-0003-1255-7183

Piming Ma − *Key Laboratory of Synthetic and Biological Colloids, Ministry of Education, School of Chemical and Material Engineering, Jiangnan University, Wuxi 214122, China*; orcid.org/0000-0002-4597-0639

Weifu Dong − *Key Laboratory of Synthetic and Biological Colloids, Ministry of Education, School of Chemical and Material Engineering, Jiangnan University, Wuxi 214122, China*; orcid.org/0000-0002-7432-8362

Complete contact information is available at:

https://doi.org/10.1021/acsami.1c13863
ACS Appl. Mater. Interfaces 2021, 13, 47134−47146

https://pubs.acs.org/10.1021/acsami.1c13863

Author Contributions

The article was written through contributions of all authors. All authors have given approval to the final version of the article.

Notes

The authors declare no competing financial interest.

■ ACKNOWLEDGMENTS

This work is financially supported by the National Natural Science Foundation of China (21875033), the Shanghai Scientific and Technological Innovation Project (18JC1410600), and the State Key Laboratory for Modification of Chemical Fibers and Polymer Materials, Donghua University.

■ REFERENCES

(1) Naguib, M.; Kurtoglu, M.; Presser, V.; Lu, J.; Niu, J.; Heon, M.; Hultman, L.; Gogotsi, Y.; Barsoum, M. W. Two-Dimensional Nanocrystals Produced by Exfoliation of Ti_3AlC_2. *Adv. Mater.* **2011**, *23*, 4248−4253.

(2) Wan, Y.-J.; Li, X.-M.; Zhu, P.-L.; Sun, R.; Wong, C.-P.; Liao, W.-H. Lightweight, Flexible MXene/Polymer Film with Simultaneously Excellent Mechanical Property and High-Performance Electromagnetic Interference Shielding. *Composites, Part A* **2020**, *130*, 105764.

(3) Wu, Z.; Shang, T.; Deng, Y.; Tao, Y.; Yang, Q. H. The Assembly of MXenes from 2D to 3D. *Adv. Sci.* **2020**, *7*, 1903077.

(4) Zhao, M. Q.; Trainor, N.; Ren, C. E.; Torelli, M.; Anasori, B.; Gogotsi, Y. Scalable Manufacturing of Large and Flexible Sheets of MXene/Graphene Heterostructures. *Adv. Mater. Technol.* **2019**, *4*, 1800639.

(5) Fan, Z.; Wang, D.; Yuan, Y.; Wang, Y.; Cheng, Z.; Liu, Y.; Xie, Z. A Lightweight and Conductive MXene/Graphene Hybrid Foam for Superior Electromagnetic Interference Shielding. *Chem. Eng. J.* **2020**, *381*, 122696.

(6) Dai, Y.; Wu, X.; Liu, Z.; Zhang, H.-B.; Yu, Z.-Z. Highly Sensitive, Robust and Anisotropic MXene Aerogels for Efficient Broadband Microwave Absorption. *Composites, Part B* **2020**, *200*, 108263.

(7) Ma, Y.; Yue, Y.; Zhang, H.; Cheng, F.; Zhao, W.; Rao, J.; Luo, S.; Wang, J.; Jiang, X.; Liu, Z.; Liu, N.; Gao, Y. 3D Synergistical MXene/Reduced Graphene Oxide Aerogel for a Piezoresistive Sensor. *ACS Nano* **2018**, *12*, 3209−3216.

(8) Wang, N.-N.; Wang, H.; Wang, Y.-Y.; Wei, Y.-H.; Si, J.-Y.; Yuen, A. C. Y.; Xie, J.-S.; Yu, B.; Zhu, S.-E.; Lu, H.-D.; Yang, W.; Chan, Q. N.; Yeoh, G.-H. Robust, Lightweight, Hydrophobic, and Fire-Retarded Polyimide/MXene Aerogels for Effective Oil/Water Separation. *ACS Appl. Mater. Interfaces* **2019**, *11*, 40512−40523.

(9) Wang, Q.-W.; Zhang, H.-B.; Liu, J.; Zhao, S.; Xie, X.; Liu, L.; Yang, R.; Koratkar, N.; Yu, Z.-Z. Multifunctional and Water-Resistant MXene-Decorated Polyester Textiles with Outstanding Electromagnetic Interference Shielding and Joule Heating Performances. *Adv. Funct. Mater.* **2019**, *29*, 1806819.

(10) Shao, L.; Xu, J.; Ma, J.; Zhai, B.; Li, Y.; Xu, R.; Ma, Z.; Zhang, G.; Wang, C.; Qiu, J. MXene/RGO Composite Aerogels with Light and High-Strength for Supercapacitor Electrode Materials. *Compos. Commun.* **2020**, *19*, 108−113.

(11) Zhou, Z.; Liu, J.; Zhang, X.; Tian, D.; Zhan, Z.; Lu, C. Ultrathin MXene/Calcium Alginate Aerogel Film for High-Performance Electromagnetic Interference Shielding. *Adv. Mater. Interfaces* **2019**, *6*, 1802040.

(12) He, P.; Cao, M.-S.; Cai, Y.-Z.; Shu, J.-C.; Cao, W.-Q.; Yuan, J. Self-Assembling Flexible 2D Carbide MXene Film with Tunable Integrated Electron Migration and Group Relaxation Toward Energy Storage and Green EMI Shielding. *Carbon* **2020**, *157*, 80−89.

(13) Wang, L.; Liu, H.; Lv, X.; Cui, G.; Gu, G. Facile Synthesis 3D Porous MXene $Ti_3C_2T_x$@RGO Composite Aerogel with Excellent Dielectric Loss and Electromagnetic Wave Absorption. *J. Alloys Compd.* **2020**, *828*, 154251.

(14) Liu, M.; Wang, Z.; Song, P.; Yang, Z.; Wang, Q. Flexible MXene/rGO/CuO Hybrid Aerogels for High Performance Acetone Sensing at Room Temperature. *Sens. Actuators, B* **2021**, *340*, 129946.

(15) Zhang, B.; Luo, C.; Zhou, G.; Pan, Z. Z.; Ma, J.; Nishihara, H.; He, Y. B.; Kang, F.; Lv, W.; Yang, Q. H. Lamellar MXene Composite Aerogels with Sandwiched Carbon Nanotubes Enable Stable Lithium−Sulfur Batteries with a High Sulfur Loading. *Adv. Funct. Mater.* **2021**, *31*, 2100793.

(16) Liu, J.; Liu, Y.; Zhang, H.-B.; Dai, Y.; Liu, Z.; Yu, Z.-Z. Superelastic and Multifunctional Graphene-Based Aerogels by Interfacial Reinforcement with Graphitized Carbon at High Temperatures. *Carbon* **2018**, *132*, 95−103.

(17) Yang, J.; Ye, Y.; Li, X.; Lü, X.; Chen, R. Flexible, Conductive, and Highly Pressure-Sensitive Graphene-Polyimide Foam for Pressure Sensor Application. *Compos. Sci. Technol.* **2018**, *164*, 187−194.

(18) Li, X.; Yin, X.; Song, C.; Han, M.; Xu, H.; Duan, W.; Cheng, L.; Zhang, L. Self-Assembly Core-Shell Graphene-Bridged Hollow MXenes Spheres 3D Foam with Ultrahigh Specific EM Absorption Performance. *Adv. Funct. Mater.* **2018**, *28*, 1803938.

(19) Cao, X.; Zhang, J.; Chen, S.; Varley, R. J.; Pan, K. 1D/2D Nanomaterials Synergistic, Compressible, and Response Rapidly 3D Graphene Aerogel for Piezoresistive Sensor. *Adv. Funct. Mater.* **2020**, *30*, 2003618.

(20) Ren, R.-P.; Wang, Z.; Ren, J.; Lv, Y.-K. Highly Compressible Polyimide/Graphene Aerogel for Efficient Oil/Water Separation. *J. Mater. Sci.* **2018**, *54*, 5918−5926.

(21) Jiang, Q.; Liao, X.; Yang, J.; Wang, G.; Chen, J.; Tian, C.; Li, G. A Two-Step Process for the Preparation of Thermoplastic Polyurethane/Graphene Aerogel Composite Foams with Multi-Stage Networks for Electromagnetic Shielding. *Compos. Commun.* **2020**, *21*, 100416.

(22) Liu, Z.; Qin, Z.; Zhao, G.; Aladejana, J. T.; Wang, H.; Huang, A.; Chen, D.; Xie, Y.; Peng, X.; Chen, T. High-Efficiency Oil/Water Absorbent Using Hydrophobic Silane-Modified Plant Fiber Sponges. *Compos. Commun.* **2021**, *25*, 100763.

(23) Li, Y.; Liu, X.; Nie, X.; Yang, W.; Wang, Y.; Yu, R.; Shui, J. Multifunctional Organic-Inorganic Hybrid Aerogel for Self-Cleaning, Heat-Insulating, and Highly Efficient Microwave Absorbing Material. *Adv. Funct. Mater.* **2019**, *29*, 1807624.

(24) Wang, K.; Lou, Z.; Wang, L.; Zhao, L.; Zhao, S.; Wang, D.; Han, W.; Jiang, K.; Shen, G. Bioinspired Interlocked Structure-Induced High Deformability for Two-Dimensional Titanium Carbide (MXene)/Natural Microcapsule-Based Flexible Pressure Sensors. *ACS Nano* **2019**, *13*, 9139−9147.

(25) Xu, X.; Wang, R.; Nie, P.; Cheng, Y.; Lu, X.; Shi, L.; Sun, J. Copper Nanowire-Based Aerogel with Tunable Pore Structure and Its Application as Flexible Pressure Sensor. *ACS Appl. Mater. Interfaces* **2017**, *9*, 14273−14280.

(26) Chen, Z.; Hu, Y.; Zhuo, H.; Liu, L.; Jing, S.; Zhong, L.; Peng, X.; Sun, R.-c. Compressible, Elastic, and Pressure-Sensitive Carbon Aerogels Derived from 2D Titanium Carbide Nanosheets and Bacterial Cellulose for Wearable Sensors. *Chem. Mater.* **2019**, *31*, 3301−3312.

(27) Khan, F. A.; Ajmal, C. M.; Bae, S.; Seo, S.; Moon, H.; Baik, S. Silver Nanoflower Decorated Graphene Oxide Sponges for Highly Sensitive Variable Stiffness Stress Sensors. *Small* **2018**, *14*, 1800549.

(28) Wu, X.; Liu, X.; Wang, J.; Huang, J.; Yang, S. Reducing Structural Defects and Oxygen-Containing Functional Groups in GO-Hybridized CNTs Aerogels: Simultaneously Improve the Electrical and Mechanical Properties to Enhance Pressure Sensitivity. *ACS Appl. Mater. Interfaces* **2018**, *10*, 39009−39017.

(29) Peng, X.; Wu, K.; Hu, Y.; Zhuo, H.; Chen, Z.; Jing, S.; Liu, Q.; Liu, C.; Zhong, L. A Mechanically Strong and Sensitive CNT/rGO-CNF Carbon Aerogel for Piezoresistive Sensors. *J. Mater. Chem. A* **2018**, *6*, 23550−23559.

(30) Zhao, X.; Wang, W.; Wang, Z.; Wang, J.; Huang, T.; Dong, J.; Zhang, Q. Flexible PEDOT:PSS/Polyimide Aerogels with Linearly

Responsive and Stable Properties for Piezoresistive Sensor Applications. *Chem. Eng. J.* **2020**, *395*, 125115.
(31) Wu, Y.-h.; Liu, H.-z.; Chen, S.; Dong, X.-c.; Wang, P.-p.; Liu, S.-q.; Lin, Y.; Wei, Y.; Liu, L. Channel Crack-Designed Gold@PU Sponge for Highly Elastic Piezoresistive Sensor with Excellent Detectability. *ACS Appl. Mater. Interfaces* **2017**, *9*, 20098−20105.
(32) Huang, J.; Li, D.; Zhao, M.; Ke, H.; Mensah, A.; Lv, P.; Tian, X.; Wei, Q. Flexible Electrically Conductive Biomass-Based Aerogels for Piezoresistive Pressure/Strain Sensors. *Chem. Eng. J.* **2019**, *373*, 1357−1366.
(33) Huang, J.; Zeng, J.; Liang, B.; Wu, J.; Li, T.; Li, Q.; Feng, F.; Feng, Q.; Rood, M. J.; Yan, Z. Multi-Arch-Structured All-Carbon Aerogels with Superelasticity and High Fatigue Resistance as Wearable Sensors. *ACS Appl. Mater. Interfaces* **2020**, *12*, 16822−16830.
(34) Wang, M.; Chen, Y.; Qin, Y.; Wang, T.; Yang, J.; Xu, F. Compressible, Fatigue Resistant, and Pressure-Sensitive Carbon Aerogels Developed with a Facile Method for Sensors and Electrodes. *ACS Sustainable Chem. Eng.* **2019**, *7*, 12726−12733.
(35) Wei, S.; Qiu, X.; An, J.; Chen, Z.; Zhang, X. Highly Sensitive, Flexible, Green Synthesized Graphene/Biomass Aerogels for Pressure Sensing Application. *Compos. Sci. Technol.* **2021**, *207*, 108730.
(36) Long, S.; Feng, Y.; He, F.; Zhao, J.; Bai, T.; Lin, H.; Cai, W.; Mao, C.; Chen, Y.; Gan, L.; Liu, J.; Ye, M.; Zeng, X.; Long, M. Biomass-Derived, Multifunctional and Wave-Layered Carbon Aerogels toward Wearable Pressure Sensors, Supercapacitors and Triboelectric Nanogenerators. *Nano Energy* **2021**, *85*, 105973.
(37) Jiang, Z.; Si, H.; Chen, X.; Liu, H.; Zhang, L.; Zhang, Y.; Gong, C.; Zhang, J. Simultaneous Enhancement of Impedance Matching and the Absorption Behavior of BN/RGO Nanocomposites for Efficiency Microwave Absorption. *Compos. Commun.* **2020**, *22*, 100503.
(38) Li, T.; Zhi, D.; Chen, Y.; Li, B.; Zhou, Z.; Meng, F. Multiaxial Electrospun Generation of Hollow Graphene Aerogel Spheres for Broadband High-Performance Microwave Absorption. *Nano Res.* **2020**, *13*, 477−484.
(39) Wang, S.; Li, D.; Zhou, Y.; Jiang, L. Hierarchical $Ti_3C_2T_x$ MXene/Ni Chain/ZnO Array Hybrid Nanostructures on Cotton Fabric for Durable Self-Cleaning and Enhanced Microwave Absorption. *ACS Nano* **2020**, *14*, 8634−8645.
(40) An, Z.; Ye, C.; Zhang, R.; Zhou, P. Flexible and Recoverable SiC Nanofiber Aerogels for Electromagnetic Wave Absorption. *Ceram. Int.* **2019**, *45*, 22793−22801.
(41) Lan, D.; Gao, Z.; Zhao, Z.; Kou, K.; Wu, H. Application Progress of Conductive Conjugated Polymers in Electromagnetic Wave Absorbing Composites. *Compos. Commun.* **2021**, *26*, 100767.
(42) Zhao, G.; Lv, H.; Zhou, Y.; Zheng, X.; Wu, C.; Xu, C. Self-Assembled Sandwich-like MXene-Derived Nanocomposites for Enhanced Electromagnetic Wave Absorption. *ACS Appl. Mater. Interfaces* **2018**, *10*, 42925−42932.
(43) Li, Y.; Li, S.; Zhang, T.; Shi, L.; Liu, S.; Zhao, Y. 3D Hierarchical Co_3O_4/Reduced Graphene Oxide/Melamine Derived Carbon Foam as a Comprehensive Microwave Absorbing. *J. Alloys Compd.* **2019**, *792*, 424−431.
(44) Zhang, K.; Lv, W.; Chen, J.; Ge, H.; Chu, C.; Tang, D. Synthesis of RGO/AC/Fe_3O_4 Composite Having 3D Hierarchically Porous Morphology for High Effective Electromagnetic Wave Absorption. *Composites, Part B* **2019**, *169*, 1−8.
(45) Lei, Y.; Yao, Z.; Li, S.; Zhou, J.; Haidry, A. A.; Liu, P. Broadband High-Performance Electromagnetic Wave Absorption of Co-Doped NiZn Ferrite/Polyaniline on MXenes. *Ceram. Int.* **2020**, *46*, 10006−10015.
(46) Li, Y.; Meng, F.; Mei, Y.; Wang, H.; Guo, Y.; Wang, Y.; Peng, F.; Huang, F.; Zhou, Z. Electrospun Generation of $Ti_3C_2T_x$ MXene@ Graphene Oxide Hybrid Aerogel Microspheres for Tunable High-Performance Microwave Absorption. *Chem. Eng. J.* **2020**, *391*, 123512.
(47) He, J.; Liu, S.; Deng, L.; Shan, D.; Cao, C.; Luo, H.; Yan, S. Tunable Electromagnetic and Enhanced Microwave Absorption Properties in $CoFe_2O_4$ Decorated Ti_3C_2 MXene Composites. *Appl. Surf. Sci.* **2020**, *504*, 144210.
(48) Liang, L.; Yang, R.; Han, G.; Feng, Y.; Zhao, B.; Zhang, R.; Wang, Y.; Liu, C. Enhanced Electromagnetic Wave-Absorbing Performance of Magnetic Nanoparticles-Anchored 2D $Ti_3C_2T_x$ MXene. *ACS Appl. Mater. Interfaces* **2020**, *12*, 2644−2654.
(49) Lusha, Z.; Zicheng, T.; Tusiime, R.; Shaofei, W.; Ningning, F.; Yifan, Z.; Hui, Z.; Yong, L. Synthesis and Electromagnetic Wave Absorbing Properties of a Polymer-Derived SiBNC Ceramic Aerogel. *Ceram. Int.* **2021**, *47*, 18984−18990.
(50) Zhao, T.; Ji, X.; Jin, W.; Xiong, C.; Ma, W.; Wang, C.; Duan, S.; Dang, A.; Li, H.; Li, T.; Shang, S.; Zhou, Z. Synthesis and Electromagnetic Wave Absorption Property of Amorphous Carbon Nanotube Networks on a 3D Graphene Aerogel/$BaFe_{12}O_{19}$ Nanocomposite. *J. Alloys Compd.* **2017**, *708*, 115−122.
(51) Guo, R.; Huo, W.; Wang, K.; Shi, D.; Wu, J.; Li, H.; Liu, H. Fabrication of Co-Zn Stannate ($Co_xZn_{1-x}SnO_3$) Hollow Balls Based 3D rGO Aerogels with Excellent Electromagnetic Wave Absorption Properties. *J. Alloys Compd.* **2020**, *845*, 156165.
(52) Fu, X.; Guo, Y.; Guan, L.; Liu, J. Three Dimensional Nylon66@ Carbon Nanotube Aerogel: A Platform for High-Performance Electromagnetic Wave Absorbing Composites. *Mater. Lett.* **2019**, *247*, 147−150.
(53) Deng, B.; Wang, L.; Xiang, Z.; Liu, Z.; Pan, F.; Lu, W. Rational Construction of MXene/Ferrite@C Hybrids with Improved Impedance Matching for High-Performance Electromagnetic Absorption Applications. *Mater. Lett.* **2021**, *284*, 129029.
(54) Xu, J.; Zhang, X.; Yuan, H.; Zhang, S.; Zhu, C.; Zhang, X.; Chen, Y. N-Doped Reduced Graphene Oxide Aerogels Containing Pod-like N-Doped Carbon Nanotubes and FeNi Nanoparticles for Electromagnetic Wave Absorption. *Carbon* **2020**, *159*, 357−365.